Journal of
Synchrotron
Radiation

ISSN 0909-0495

Received 27 January 2010
Accepted 26 March 2010

Comparative study of multilayers used in monochromators for synchrotron-based coherent hard X-ray imaging

A. Rack,[a,b]* T. Weitkamp,[a,b]* M. Riotte,[b] D. Grigoriev,[b] T. Rack,[b] L. Helfen,[b] T. Baumbach,[b] R. Dietsch,[c] T. Holz,[c] M. Krämer,[c] F. Siewert,[d] M. Meduňa,[e] P. Cloetens[a] and E. Ziegler[a]

[a]European Synchrotron Radiation Facility, 38043 Grenoble Cedex, France, [b]Institute for Synchrotron Radiation – ANKA, Karlsruhe Institute of Technology, 76021 Karlsruhe, Germany, [c]AXO Dresden GmbH, 01809 Heidenau, Germany, [d]Helmholtz Zentrum Berlin/BESSY-II, 12489 Berlin, Germany, and [e]Department of Condensed Matter Physics, Masaryk University, 61137 Brno, Czech Republic. E-mail: arack@snafu.de, weitkamp@esrf.fr

A systematic study is presented in which multilayers of different composition (W/Si, Mo/Si, Pd/B_4C), periodicity (from 2.5 to 5.5 nm) and number of layers have been characterized. In particular, the intrinsic quality (roughness and reflectivity) as well as the performance (homogeneity and coherence of the outgoing beam) as a monochromator for synchrotron radiation hard X-ray micro-imaging are investigated. The results indicate that the material composition is the dominating factor for the performance. By helping scientists and engineers specify the design parameters of multilayer monochromators, these results can contribute to a better exploitation of the advantages of multilayer monochromators over crystal-based devices; *i.e.* larger spectral bandwidth and high photon flux density, which are particularly useful for synchrotron-based micro-radiography and -tomography.

Keywords: multilayer mirrors; X-rays; X-ray optics; coherence; X-ray monochromators; X-ray imaging; X-ray phase contrast.

1. Introduction

The use of X-rays for imaging techniques allows for probing the inner structure of a specimen in a widely non-destructive manner. In combination with tomographic methods, three-dimensional images can be recorded which are the basis for countless medical diagnoses as well as numerous applications in materials research, life science, archaeology, paleontology or non-destructive evaluation (for a detailed review see, for example, Stock, 1999, 2008; Baruchel *et al.*, 2002, 2006; Hsieh, 2009; Banhart, 2008). During the 1980s, laboratory methods had already pushed the reachable spatial imaging resolution into the micrometer range (Elliott & Dover, 1982; Flannery *et al.*, 1987), partially driven by successful applications of computed tomography in non-medical fields (Reimers & Goebbels, 1983). In parallel, X-ray optics based on multilayer structures demonstrated their potential, and discussions about synchrotron-based X-ray imaging using these structures began (Spiller, 1980; Underwood & Barbee, 1981).

The development of synchrotron-based micro-imaging goes back to the same decade (*cf.* Spanne & Rivers, 1987; Kinney *et al.*, 1989; Bonse *et al.*, 1989; Graeff & Engelke, 1991). The method was established during the 1990s supported by the third-generation light sources starting their operation as well as high-resolution detection schemes becoming widely available (Koch, 1994; Bonse & Busch, 1996; Cloetens *et al.*, 1996; Raven *et al.*, 1996; Lee *et al.*, 1997; Spanne *et al.*, 1999). By the end of that decade, spatial resolutions in the (sub-)micrometer range were reached by combining thin transparent single-crystal scintillators with diffraction-limited visible-light microscopy objectives (Koch *et al.*, 1998). Recently, imaging experiments with a spatio-temporal resolution down to the micrometer–microsecond range were published (Wang *et al.*, 2008; Rack *et al.*, 2009*a*). The first (double-)multilayer monochromators used have been reported since the late 1980s (Pianetta *et al.*, 1986; Golub *et al.*, 1989; Graeff & Engelke, 1991; Deschamps *et al.*, 1995; Sammar *et al.*, 1997).

The performance of a micro-imaging facility at a synchrotron light source is directly connected to the available monochromatic photon flux density and coherence properties. Using a monochromatic beam increases the contrast by reducing artifacts as well as giving access to more sophisticated contrast modalities such as inline phase contrast or holotomography (Cloetens *et al.*, 1999). An example of a thorough comparative study between synchrotron radiation and laboratory X-ray sources for imaging (mammography)

was published by Moeckli *et al.* (2000). The available photon flux density should be high for several reasons: the required exposure time per image has to be kept reasonably short (*e.g.* for a full-field micro-tomography scan, commonly 1500 angular projection images have to be acquired) not only because of the limited beam time available; mechanical instabilities, *e.g.* owing to thermal drifts, have to be considered as well. Furthermore, the detectable density-related material contrast depends on the number of photons in a strongly non-linear manner, *e.g.* to double the detection limit an increase of the photon number by a factor of four is required (Flannery & Roberge, 1987). As a quantitative example of the required photon flux densities, let us consider a micro-tomography scan of a Si specimen (1 mm diameter) with 2 µm spatial resolution: with a monochromatic photon flux density in the range of 10^{10} photons s^{-1} mm^{-2} and 10 h total exposure time (1 µm effective pixel size of the detector, 1000 pixels per detector line, 3000 projections images with a dynamic range of 10000:1) a material contrast of $\Delta\mu/\mu \simeq 4\%$ can be detected (where μ is the X-ray attenuation coefficient) (Brooks & DiChiro, 1976). Finally, the efficiency of an indirect pixel detector usually decreases when the spatial resolution is increased. This is due to the thin scintillating films required to fit in the depth of focus of microscope objectives with large numerical apertures [*e.g.* for a spatial resolution around 1 µm a 5 µm thin scintillator crystal is required; in the case of $Lu_3Al_5O_{12}$ (LAG) such a luminescence screen absorbs only 25% of the photons at an X-ray energy of 15 keV (Koch *et al.*, 1998; Rack *et al.*, 2008, 2009)].

In comparison with crystal monochromators, multilayers have some distinct advantages. First, the multilayer period (and thus the reflected photon wavelength) can be adjusted to arbitrary values, in particular to wavelengths above 1 nm that are hardly or not accessible by crystals. Second, the typical energy bandwidth $\Delta E/E$ of a multilayer is one to two orders of magnitude larger than that of a crystal. This is advantageous if the X-ray source emits a similar or larger energy band. In this way the multilayer reflects a larger portion of the energy spectrum leading to increased integral intensity. Third, certain curved geometries can be manufactured more easily with multilayers that are deposited on bent or curved substrates than bending a crystal to small radii of curvature. Multilayers are also employed to build sophisticated X-ray optics such as multilayer Laue lenses (Conley *et al.*, 2008).

To further increase the available monochromatic photon flux density, bendable multilayers have been used, at the expense of degrading the coherence properties of the beam. Hence, bending is commonly used only in combination with absorption contrast imaging (Ziegler *et al.*, 2001; Wang *et al.*, 2007; Rack *et al.*, 2008, 2009, 2010).

Typical methods of multilayer fabrications are magnetron sputter deposition, large-area pulsed-laser deposition and dual ion-beam deposition technologies. Depending on the multilayer structure, especially the selected elements and the available resources, one of these methods is chosen (Liu *et al.*, 2001; Dietsch *et al.*, 2002; Morawe *et al.*, 2007; Störmer *et al.*, 2008).

The multilayer composition is selected depending on the photon energy range used but also considering aspects of the application set-up (vacuum, gas, air), heat load and temporal stability. Chemical behavior such as phase formations, inter-diffusion and others has to be considered as well. Typical material combinations are, for example, W/Si, Mo/Si, Pd/B_4C, which are presented in this article, but also Ni/C, Cr/Sc, W/B_4C, La/B_4C and numerous others (Ziegler, 1995; Montcalm *et al.*, 1996). For special applications, even C/C multilayers have been fabricated with interfaces solely defined by the different C density in neighboring layers (Dietsch *et al.*, 1995).

The number of multilayer monochromators running at synchrotrons worldwide is constantly increasing, though still limited compared with crystal monochromators. Installed systems reported in the literature which are used for imaging applications, in-house fabricated or commercially manufactured, are for example (in no particular order): at the European Synchrotron Radiation Facility (ESRF) a single mirror with three multilayer stripes at beamline ID19 [W/B_4C, 150 bi-layers, *d*-spacing = 2.5 nm, 2 × Ru/B_4C with 40 bi-layers/*d*-spacing = 6.0 nm and 65 bi-layers/*d*-spacing = 4.0 nm (http://www.esrf.eu/, last visit 2010)] as well as a double-multilayer monochromator (DMM) at BM05 [Ru/B_4C, 70 bi-layers, *d*-spacing = 4.0 nm (Bigault *et al.*, 2003; Ziegler *et al.*, 2004)]; the TOMCAT beamline at the Swiss Light Source installed a DMM with two stripes [Ru/C and W/Si, each 100 layers, *d*-spacing = 2.0 nm and 4.0 nm, respectively (Stampanoni *et al.*, 2007)]; at the Advanced Photon Source (APS) a DMM is installed at the micro-imaging station 2-BM [W/B_4C, 200 bi-layers, *d*-spacing = 1.38 nm (Chu *et al.*, 2002)]; the BESSY-II synchrotron light source runs a DMM at the BAM*line* [W/Si, 150 bi-layers, *d*-spacing = 2.88 nm (Görner *et al.*, 2001; Riesemeier *et al.*, 2005; Rack *et al.*, 2008)]; two systems are installed at the ANKA storage ring, one DMM at the FLUO beamline [W/Si, 200 bi-layers, *d*-spacing = 2.7 nm (Simon *et al.*, 2003)] and another one at the TopoTomo beamline [W/Si and Pd/B_4C, 250 layers, *d*-spacing = 2.5 nm, (Rack *et al.*, 2009*b*; Rack *et al.*, 2010)]; different mirrors are installed at CHESS [*e.g.* Mo/B_4C with 1.5 nm and 3.0 nm *d*-spacing for imaging (Kazimirov *et al.*, 2006)]; a multilayer monochromator is installed at the tomography beamline of the CAMD synchrotron [W/B_4C, >200 bi-layers, *d*-spacing = 2.0 nm (Ham *et al.*, 2002)] as well as at the tomography beamline 8.3.2 of the Advanced Light Source (W/B_4C), and at the Pohang Light Source (PLS) the 1B2/microprobe beamline uses a DMM [W/Si, 100 bi-layers, *d*-spacing = 2.5 nm (Jheon *et al.*, 2006)].

2. Motivation

As Spiller (1988) put it, 'multilayer films for X-rays can be seen as an extension of natural crystals to larger lattice spacings or of optical coatings to shorter wavelengths'. The great advantage of multilayer structures over crystal lattices for diffractive monochromatization of X-rays is the higher flux density of the exit wave, but other properties of the beam are

affected as well. For example, the spectral bandwidth of the exit beam when using a multilayer monochromator is larger than that of a crystal monochromator (typical values $\Delta E/E \simeq 10^{-3}$–$10^{-2}$ *versus* $\Delta E/E \simeq 10^{-5}$–$10^{-4}$). However, the fact that the multilayer parameters such as period thickness (d-spacing), thickness ratio Γ, potential grading of the period, materials combination and number of layers can be freely chosen allows the spectral bandpass to be tailored to a certain degree to match the needs of the intended application. Even with techniques such as absorption spectroscopy, which call for the use of a crystal monochromator because of the required energy resolution, multilayer systems can be useful for the pre-monochromatization in combination with beam steering or for focusing.

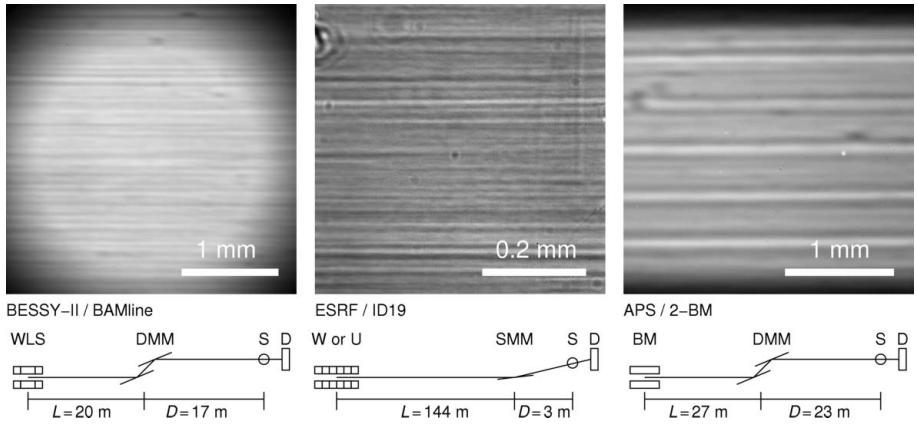

Figure 1
Examples of stripe modulations in the flat-field image after reflection by multilayer mirrors of different materials, period d and number N of bi-layers, in use at different beamlines around the globe. (Note that these are not the multilayer samples which are under investigation in this paper.) The sketches below show the essential layout elements of each beamline: source (WLS: wavelength shifter; W: wiggler; U: undulator; BM: bending magnet), monochromator (DMM: double multilayer monochromator; SMM: single multilayer monochromator), and the distances L and D between source, multilayer and experimental station (S: sample; D: detector). The sketches do not show filters, windows, *etc*. Left: W/Si, $N = 150$, $d = 2.88$ nm at the BAM*line*, BESSY-II. Center: Ru/B_4C, $N = 65$, $d = 3.92$ nm, at ESRF beamline ID19. Right: W/B_4C, $N = 200$, $d = 1.38$ nm, at APS beamline 2-BM.

Furthermore, the grazing-incidence angle (typical values in the range from 0.2° to 1.0°) leads to a number of additional aspects to be considered, *i.e.* the reduced aperture in the direction of the diffraction vector, and therefore a reduced beam size with respect to crystal monochromators of similar dimensions of the reflective surface. This results in the need to extend the multilayer mirror length, within limits imposed by present fabrication technology, mechanics, space and costs (currently, multilayers up to 1 m in length can be produced; see, for example, Morawe *et al.*, 2007; Morawe & Peffen, 2009; Störmer *et al.*, 2008). The corresponding large footprint on a long mirror reduces the effective power density, which has the advantage of allowing one to cope with higher heat loads. Also owing to the grazing-incidence angle, for a DMM a relatively long distance is required between the two multilayer mirrors to ensure a reasonably large offset between the primary and the monochromatic beam needed to effectively block the primary beam with a beam stop. The large and relatively heavy design that results from these requirements, particularly if a fixed-exit design is required, means that it is usually not possible to perform quick scans of the photon energy with a multilayer monochromator. For the instrumentation of a beamline the installation of a multilayer monochromator requires attenuators to block lower energies passing by total external reflection (different sets of attenuators must be inserted as a function of the photon energy selected with the monochromator).

The most important side effect of multilayer monochromatization on micro-imaging applications is the irregular stripe pattern induced in the beam profile. Typical examples of these patterns can be found in Fig. 1, acquired at different synchrotron light sources worldwide. The stripes cause artifacts, restrict the full exploitation of the dynamic range of the image detector used and lead to different signal-to-noise ratios within the data. Furthermore, owing to the finite spatial resolution of the detector as well as the influence of the probed specimen on the beam propagation, the stripes can often not be completely eliminated by a flat-field correction procedure, which causes ring artifacts in tomography (Sijbers & Postnov, 2004). Another effect degrading the beam quality is the loss of spatial coherence in the reflected beam, owing to imperfections of the multilayer monochromator. This loss causes contrast degradation in phase-sensitive X-ray imaging. Techniques to alleviate negative side effects of multilayer use exist, but they frequently aggravate other such effects. For example, a diffuser in the beam path is an efficient means of eliminating unwanted stripes, but it has a devastating effect on the spatial coherence. In order to reduce the unwanted effects of the multilayer reflection on the beam profile, strict requirements on surface roughness and figure errors must be met.

A simple attempt to describe the origin of the stripe modulation is sketched in Fig. 2. The basic assumption is that the multilayer coating reproduces the underlying surface shape of the substrate. Given this, the figure errors introduce phase shifts when a plane wavefront is reflected owing to the difference in optical path length. These phase shifts are then transformed into intensity modulations by the propagation of the beam (Cloetens *et al.*, 1996). This can be described quantitatively (Ziegler *et al.*, 1999) by the relationships

$$\left.\begin{aligned} \varphi(x) &= -(4\pi/\lambda)h(x)\sin\theta \\ 2d\sin\theta &= \lambda \end{aligned}\right\} \quad \varphi(x) = -2\pi h(x)/d\,. \qquad (1)$$

Here, λ denotes the X-ray wavelength, d the bi-layer period, θ the incidence angle, h the height variation of the multilayer surface, x the position coordinate along the multilayer surface,

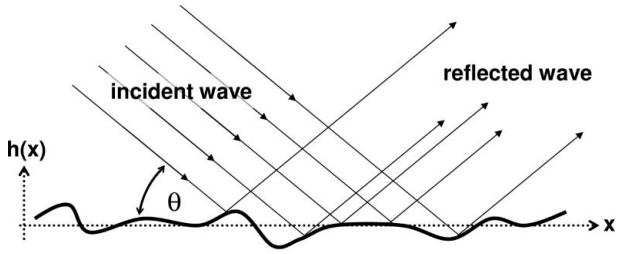

Figure 2
A simple model to explain the origin of the stripe pattern in the beam profile downstream of a multilayer monochromator (*cf.* Fig. 1). Assuming that the multilayer coating reproduces the underlying surface shape of the substrate, intensity stripes are caused by figure errors of the substrate which introduce phase shifts (h: height variation of the multilayer surface; x: position coordinate along the multilayer surface; θ: incidence angle). These shifts are transformed into intensity modulations by the propagation of the beam.

and φ the phase shift of outgoing rays reflected by parts of the multilayer with a height difference of h (*cf.* Fig. 2). The degradation of beam coherence properties is not covered explicitly within this model. Generally, coherence degradation is thought to be due to imperfections of the multilayer (roughness of the top layer surface and/or layer interfaces, bulk defects of the material). A formalism relating the performance of multilayer mirrors to their structural quality would obviously be desirable. For X-ray mirrors working in the total external reflection regime, there are a few publications relating the surface characteristics to the resulting beam quality in a quantitative and rigorous manner (Schelokov *et al.*, 1996; Souvorov *et al.*, 2002; Yamauchi *et al.*, 2005; Kewish *et al.*, 2007). However, for multilayer optics, there is as yet no sound model correlating the structure parameters with the X-ray beam properties.

The primary advantage of the multilayer reflection compared with the crystal lattice reflection is the higher photon flux density at the sample because of the larger spectral bandpass. The disadvantage lies in the stronger modifications on the beam profile, a major issue for micro-imaging applications where multilayers are required to deliver high photon flux density. In this article a study will be presented and discussed which investigates the influence of the different multilayer parameters such as d-spacing, number of layers and materials composition. While this paper does not aim at developing a model describing the correlation between structure parameters and beam properties, we expect the results presented here to extend the knowledge on multilayers and their potential for X-ray imaging applications (Spiller *et al.*, 1993; Spiller, 1994; Harvey, 1995).

3. Methods

In this section the methods applied to characterize the multilayer structures (and their substrates) in terms of roughness and micro-imaging performance are briefly introduced with their corresponding parameters. A description of the multilayer structures under investigation can be found in §4, and detailed presentation of the results in §5.

3.1. Surface metrology

The imaging properties of a multilayer optical device are defined by the surface properties of the substrate as the deposited multilayers only change these properties by minor values in the nanometer range (Mancini & Bilderback, 1983). In addition to the surface figure, the roughness of the substrate is of high importance as it cannot usually be compensated by the multilayer structure. It is even reproduced to a certain degree by the multilayer surfaces and interfaces (Gawlitza *et al.*, 2008). Three spatial regions of roughness are commonly regarded: the low-spatial-frequency roughness (LSFR) with modulation periods of more than $\sim$1 mm, the mid-spatial-frequency roughness (MSFR) down to roughly 1 µm, and the high-spatial-frequency roughness (HSFR) in the nanometer range (Harvey, 1995). LSFR can be considered as figure deviations and leads to imaging errors, while MSFR causes diffuse scattering, reducing the image contrast and blurring of the image. Finally, HSFR leads to diffuse scattering outside the image resulting in a lower reflectance of the mirror. This means that the initial state of substrate micro-roughness over a wide range of spatial frequency (scales) has to be checked for multilayer production. In order to achieve this, multiple measurement techniques can be applied, such as white-light interferometry or atomic force microscopy scans, which show the nanometer range structure, though in a rather limited area.

Characterization of the substrate surfaces and the multilayer surfaces was carried out at the metrology laboratory of the BESSY-II light source, Helmholtz Zentrum Berlin für Materialien und Energie, Germany (Siewert *et al.*, 2005). For determining the bending radius as well as the slope errors, the in-house development BESSY-NOM (nanometer-optical component measuring machine) was employed. Here, by combining a long trace profiler head (LTP-III) with an autocollimation telescope, a sensitivity approximately one order of magnitude higher compared with a standard LTP can be achieved (Siewert *et al.*, 2004). Using the NOM, 20 mm line scans were performed with a lateral resolution of 2 mm. The micro-roughness (high spatial frequency roughness) was measured using a white-light interference microscope (Micromap Promap 520) with 20× and 50× magnification. In order to check for the long-term stability of the multilayer coatings, measurements were repeated two years after the deposition (in the meantime, the mirrors were kept in air).

3.2. Specular and non-specular X-ray reflectivity

X-ray reflectivity methods investigate atomic-scale roughness of surfaces and interfaces. The roughness correlation properties can be determined from the atomic to micrometer scale (Pietsch *et al.*, 2004). Illuminating an area of several square millimeters ensures statistical relevance. Two different experimental techniques were used for the characterization of the multilayer roughness: the specular X-ray reflectivity (XRR) and the non-specular XRR.

From the measurements of specular XRR the root-mean-square (r.m.s.) roughness of interfaces and surfaces and the layer thicknesses were extracted. The measurements were

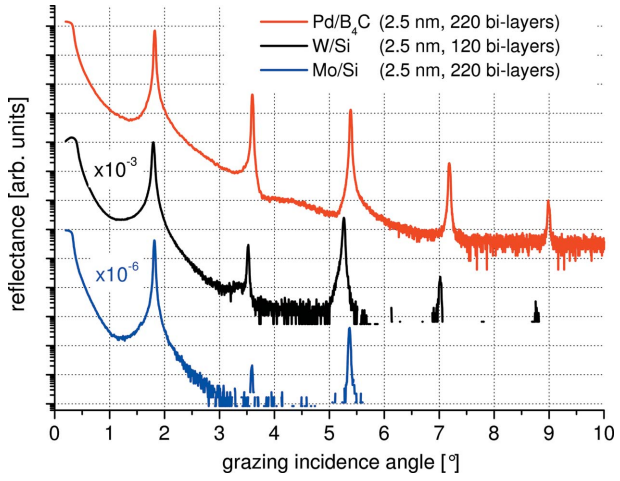

Figure 3
Reflectivity scans using Cu $K\alpha$ radiation (twin-mirror arrangement) on selected multilayer mirrors: Pd/B_4C with 220 bi-layers (sample 1680), W/Si with 120 bi-layers (sample 1531) and Mo/Si with 220 bi-layers (sample 1574), all 2.5 nm nominal d-spacing. See also Figs. 8 and 9. Curves for W/Si and Mo/Si are shifted for better visibility.

performed by AXO Dresden GmbH using a laboratory diffractometer with Cu $K\alpha$ radiation (8.04 keV) in a so-called twin-mirror arrangement (*cf.* Fig. 3) (Holz *et al.*, 2000).

For the measurements of non-specular XRR a grazing-incidence small-angle X-ray scattering (GISAXS) set-up was chosen. While this technique requires high intensities as well as specific equipment, it allows scattering to be measured in the full range of parallel momentum transfer (Salditt *et al.*, 1994). Details about the set-up used as well as the raw data are published elsewhere (Riotte, 2008).

Since the non-specular XRR signal (diffuse scattering) is determined mainly by the correlation function of the interface roughness profiles (Holý & Baumbach, 1994), we have extracted in this way the lateral and vertical roughness correlation lengths and the Hurst factor H (fractal dimension $= 3 - H$) for each multilayer sample. For this purpose we have assumed a simplified roughness model using a Ming model for the inter-plane correlation function [equation (11.28) of Pietsch *et al.* (2004)]. The in-plane correlation function is taken according to the fractal roughness model with exponential shape [equation (11.27) of Pietsch *et al.* (2004)]. The interface roughness, material density and thickness of the individual layers obtained from specular XRR simulations were taken as a fixed input for the simulations of the diffuse scattering. The measurements were performed at the SCD (single-crystal diffraction) beamline of the synchrotron light source ANKA in Karlsruhe (Germany) at a photon energy of 15 keV (http://ankaweb.fzk.de/, last visit 2010).

3.3. Full-field imaging

Measurements of the two-dimensional intensity distribution in a transverse plane several meters behind the reflection of a monochromatic X-ray beam from each multilayer test substrate were performed at beamline BM05 of the European Synchrotron Radiation Facility (ESRF). BM05 is a bending-magnet beamline particularly suited for optics tests (Ziegler *et al.*, 2004). For the experiment, the multilayer was mounted on the available vertical reflectometer, located 35 m from the source [vertical source size (FWHM): 80 µm]. The primary slits of the beamline (25 m from the source) were set to a gap size of 1.5 mm × 1.5 mm. The Si-111 crystals of the double-crystal monochromator (DCM; 27.2 m away from the source) were used to select an X-ray energy of 18 keV. The multilayer was aligned in order to reflect the impinging monochromatic beam upward onto an (indirect) high-resolution X-ray pixel detector positioned 5.4 m downstream of the reflectometer. The detector consisted of a 11 µm-thin Eu-doped $Lu_3Al_5O_{12}$ (LAG:Eu) scintillating single crystal on top of a 170 µm-thick undoped $Y_3Al_5O_{12}$ (YAG) substrate. Its luminescence image was projected by a combination of a 10× microscope objective [0.4 numerical aperture (NA)] and 2× eyepiece onto a 'FReLoN 2000'-type CCD camera (2048 × 2048 pixels, 14 µm pixel size). The resulting effective pixel size was 0.68 µm with 1.4 mm × 1.4 mm field of view. Scans of the X-ray energy around the central value of 18 keV were made with the DCM to determine the accepted spectral bandwidth of the multilayer reflection and, to a certain degree, simulate polychromatic illumination. By adding up the images obtained for different energies selected by the DCM, we obtained images that emulated polychromatic illumination. These will be referred to as 'pseudo-polychromatic illumination' in the rest of this paper.

A similar set-up but without a crystal monochromator was used at beamline TopoTomo of the ANKA light source (Karlsruhe, Germany) to determine the influence of the multilayer reflection on the achievable spatial imaging resolution (Rack *et al.*, 2009*b*). The white radiation from the bending magnet [source size (h × v): 0.5 mm × 0.14 mm, FWHM] was filtered by a 0.5 mm-thick Be exit window and by a 1 mm-thick Si wafer in order to get rid of lower photon energies and to reduce the heat load on the multilayer structures. The latter were mounted on a sample stage commonly used for Laue (transmission) white-beam topography, approximately 30 m away from the source (Danilewsky *et al.*, 2003, 2008). The multilayers were aligned with respect to the incoming X-ray beam using the totally reflected beam. In order to determine the spatial resolution, a test pattern (Xradia, model X500-200-30) was imaged using the white beam as well as the reflected beam (18 keV). As a detector, we used the BAM*line* macroscope available at the beamline. It consists of a Rodenstock TV-Heliflex objective (f = 50 mm, maximum NA = 0.45), a Nikkor 180/2.8 ED (f = 180 mm) objective used as a tube lens, a pco.4000 CCD camera (4008 × 2672 pixels, 9 µm in size) and a 40 µm-thick polished $CdWO_4$ (CWO) scintillating single crystal glued on top of a 0.5 mm-thick undoped $Y_3Al_5O_{12}$ substrate (3.6× magnification, 2.5 µm effective pixel size) (Nagornaya *et al.*, 2005; Rack *et al.*, 2009*b*). The distance between the multilayer and the test pattern was approximately 1 m, and that between the detector and the test pattern approximately 0.3 m. Hence, the acquired images show absorption as well as phase contrast.

3.4. Talbot imaging

In order to measure the influence of the multilayer reflection on the spatial coherence properties of the X-ray photon beam, the ESRF beamline ID19 was chosen because of its long distance between source and experimental station of roughly 150 m (Cloetens *et al.*, 1999). Additionally, the large hutch allows for realising relatively long propagation distances between the multilayer and the imaged object of around 5 m. For the experiment, both ID19 undulators were used together with a 1 mm Al absorption filter. An X-ray photon energy of 18 keV was selected by the vertically deflecting Si-111 DCM of the beamline. The multilayers were mounted in upward-deflecting geometry on a sample manipulator located close to the beam entrance of the ID19 experimental hutch, commonly used for high-resolution tomography. Again, the totally reflected beam was used in order to align the multilayers with respect to the incoming monochromatic beam and to help center the detector on the reflected beam from the multilayer. A set of two-dimensional phase-grating structures [Si, periodicity a = 2, 3, 4, 6, 8 µm, fabricated by means of electron beam lithography (David & Hambach, 1999)] and a Siemens star test structure were mounted on a second sample manipulator, commonly used for moderate resolution tomography, at approximately 5 m distance to the multilayers. The high-resolution indirect image detector consisted of a 10× microscope objective (0.3 NA, with protective lead glass), a 2× eyepiece, a 6.6 µm-thin Eu-doped $Gd_3Ga_5O_{12}$ (GGG:Eu) scintillating single crystal on top of an undoped $Gd_3Ga_5O_{12}$ substrate and the FReLoN 2k type CCD camera (2048 × 2048 pixels, 14 µm in size, 0.7 µm effective pixel size) (Labiche *et al.*, 2007). The detector was mounted on a linear translation stage allowing motion parallel to the beam over a travel range of slightly less than 1 m. By measuring the contrast of the phase gratings within the images acquired at different distances between detector and specimen it is then possible to quantitatively compare the coherence properties of the beam as reflected by the multilayers and the DCM or only the DCM (Cloetens *et al.*, 1997; Guigay *et al.*, 2004; Kluender *et al.*, 2009; Diaz *et al.*, 2010).

4. Multilayer samples

The modifications on the incoming beam profile are the major drawback of multilayer reflections for monochromatization in comparison with other concepts. Based on the present growth methods as well as raw materials which experimentally demonstrated a level of perfection, the following tunable characteristics were varied for further optimization: the material composition of the multilayers, their d-spacing and number of bi-layers N.

4.1. Substrates

Commercial one-sided superpolished silicon single crystals (General Optics, Gooch & Housego) were applied as substrates for the multilayers presented here. The substrate diameter was 25.40 mm with a thickness of 6.35 mm and surface roughness of around S_q = 0.10–0.15 nm. The serial numbers assigned by the manufacturer are given in Table 2.

Table 1
Matrix overview of the samples listed in Table 2, sorted by materials and bi-layer period.

Values shown in the main part of the table are the numbers of periods N. The nominal value for Γ is 0.5 (thickness ratio).

	Materials		
d (nm)	Mo/Si	W/Si	Pd/B_4C
2.5	220	120	220
4.0	80	–	30, 60
5.5	50	–	–

Table 2
List of samples and specifications.

The values for the period thickness d were determined by fitting X-ray reflectivity curves taken with Cu $K\alpha$ radiation near the center of the mirror. N is the number of bi-layers, R_8^{exp} the peak reflectivity as taken from the laboratory X-ray reflectivity scans (Cu $K\alpha$ radiation), R_8^{calc} and R_{18}^{calc} are the peak reflectivities for perfect multilayers (zero interdiffusion thickness, and assuming literature values of the bulk materials for the densities) on a Si substrate as calculated with the CXRO online tool for photon energies of 8 keV and 18 keV, respectively (http://www-cxro.lbl.gov/, last visit 2010).

Serial number	Materials	N	d (nm)	R_8^{exp}	R_8^{calc}	R_{18}^{calc}
1531	W/Si	120	2.528	–†	76%	78%
1574	Mo/Si	220	2.478	>45%†	77%	93%
1601	Mo/Si	80	3.975	70%	77%	93%
1609	Mo/Si	50	5.492	75%	76%	93%
1680	Pd/B_4C	220	2.468	>50%†	76%	93%
1681	Pd/B_4C	60	4.002	70%	76%	93%
1685	Pd/B_4C	30	3.982	61%	70%	86%

† Exact quantification was (partially) not possible owing to experimental limitations.

4.2. Coatings

Various multilayer structures were deposited on these substrates by means of magnetron sputtering. The parameters of the multilayer systems were arranged in such a way that the influence of each parameter could be studied without the influence of the others (*cf.* Table 1). Table 2 shows the sample materials as well as the number of bi-layers and the period thickness. The period thickness was determined by XRR measurements using a laboratory diffractometer and Cu $K\alpha$ radiation (8.04 keV) in a twin-mirror arrangement (Holz *et al.*, 2000). A few example XRR curves are plotted in Fig. 3. The period thicknesses were determined using the software *IMD* (Windt, 1998) and in-house software. We note that the measured peak reflectivities as taken from the laboratory scans are similar to those calculated for Cu $K\alpha$ radiation. Detailed analysis especially of the surface and (correlated) interface roughnesses with the same data was then performed using a special software and method as described in §3.2.

5. Results

The results presented in this section are roughly arranged with respect to the methods used to characterize the multilayer

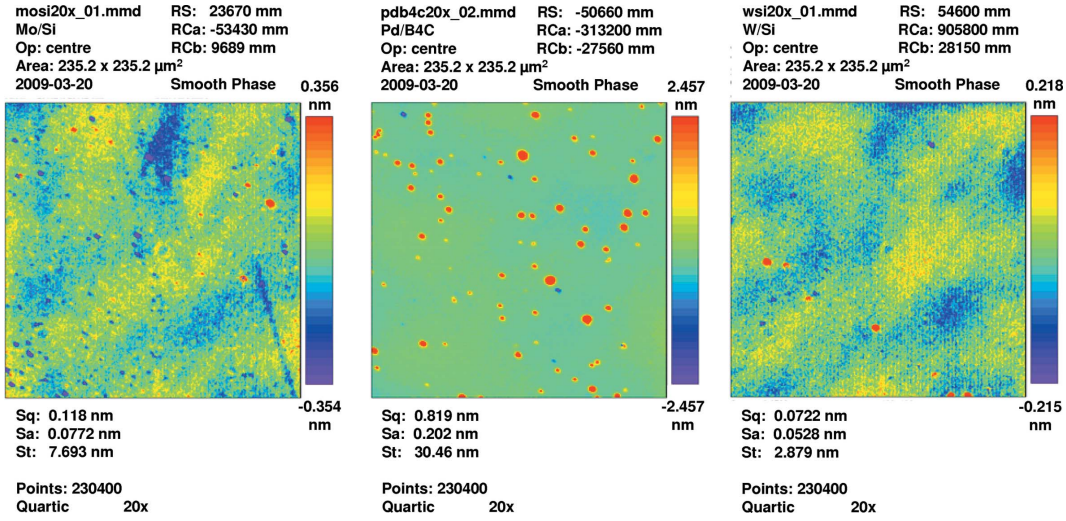

Figure 4
Micro-roughness (high spatial frequency, measured with a Micromap Promap 520 interference microscope) of the substrate with Mo/Si multilayer (left), Pd/B_4C multilayer (middle) and W/Si multilayer coating (right), magnification 20× (see also Tables 1 and 2).

structures as well as their substrates. The main goal is to give a detailed picture of the multilayers' characteristics in order to identify potential parameters for further improvement rather than trying to fully evaluate the origin of the beam profile modulations caused by the reflection on a multilayer mirror.

5.1. Metrology

The samples were characterized before and after coating as well as two years after coating. Selected micro-maps showing the high-frequency surface roughness of coated substrates can be found in Fig. 4, and exemplarily the initial state in direct comparison with a coated substrate in Fig. 5.

The surface polishing level of the bare substrates was found to be almost identical. The high-spatial-frequency micro-roughness was found to be in the range 0.10 nm r.m.s. (magnification 20×)/0.15 nm r.m.s. (magnification 50×) and the figure error in the 1.4–14.5 nm range (peak-to-valley). This corresponds to a flatness equal to or better than $\lambda/40$ (λ = 633 nm). After subtracting a best-fit sphere, a residual slope deviation of 0.15 to 0.8 µrad r.m.s. remains (corresponding to a peak-to-valley residual figure error of between 0.8 and 2.2 nm). The radius of curvature is commonly in the −5 km (convex) range.

The surface roughness of the multilayer coatings does not show a significant difference (*cf.* Figs. 4 and 5, taken two years after the coating) except for Pd/B_4C. Here, a kind of spike structure appears on the top of the coating. The fraction of the spikes on the whole surface of the coating is of the order of 2% or less. An inspection of the profile roughness, at the Pd/B_4C coated sample, showed values in the range around $R_t = 0.1$ nm r.m.s. Hence, one can assume the effect of the spikes to be negligible.

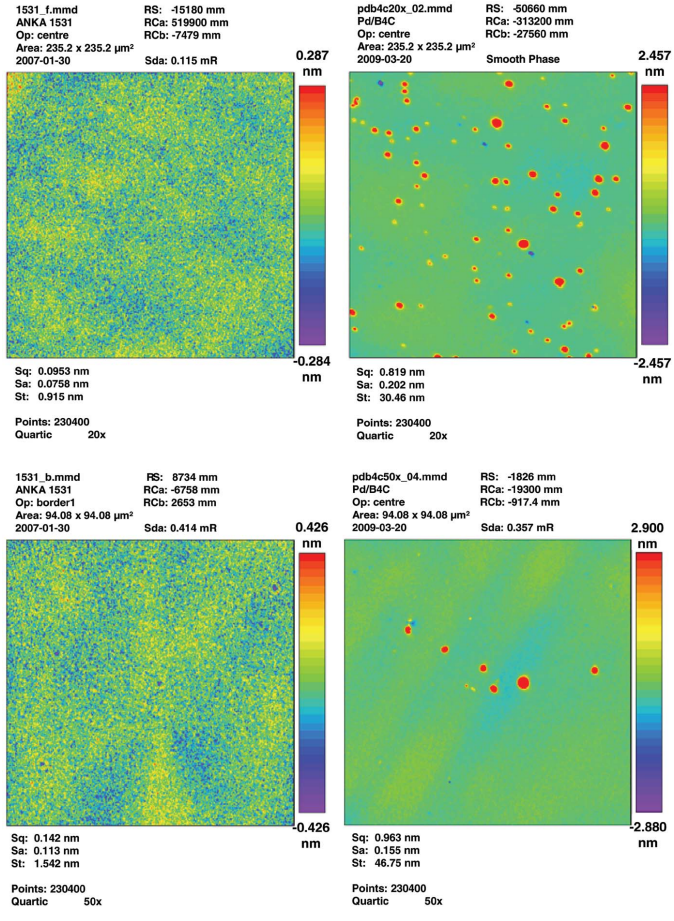

Figure 5
Micro-roughness (measured with a Micromap Promap 520 interference microscope) of one of the test substrates in its initial state (left, sample 1531; top: 20×; bottom: 50× magnification); right side: final state of one of the Pd/B_4C multilayer coatings (top: 20×; bottom: 50× magnification) (see also Tables 1 and 2).

Table 3
Surface and interface roughness including the roughness correlation properties for the seven samples investigated.

The values (all given in Å) were obtained by fitting specular and non-specular X-ray reflectivity data. The roughness of the substrate was measured as 1.5 Å.

Sample	Material	Roughness A	Roughness B	Average A, B	Surface	L_{vert} (±150)	L_{lat} (±15)	H (±0.05)
1680	Pd/B_4C	2.8	2.5	2.6	3.8	1100	105	0.80
1685	Pd/B_4C	2.9	2.4	2.6	3.2	1100	85	0.99
1681	Pd/B_4C	3.0	2.6	2.8	2.9	1100	100	0.93
1531	W/Si	3.0	2.8	2.9	3.8	700	129	0.75
1574	Mo/Si	2.9	2.9	2.9	3.8	700	115	0.68
1609	Mo/Si	3.2	3.1	3.2	6.5	700	110	0.92
1601	Mo/Si	3.6	3.2	3.4	3.8	700	120	0.77

5.2. Interface and surface roughness

As a result of the specular XRR measurements and subsequent analysis we were able to determine: (i) an r.m.s. roughness for material A (averaged over all layers), (ii) an r.m.s. roughness for material B (averaged over all layers), (iii) the average of A and B, and (iv) a surface roughness. From the non-specular XRR measurements we could extract: (v) a lateral correlation of roughness, L_{lat}, (vi) a vertical correlation of roughness, L_{vert}, and (vii) the Hurst factor, H (fractal dimension). Table 3 shows the results.

Concerning the roughness characteristics (i)–(vi), a systematic dependence was found concerning the chemical composition. All samples made from the same material show similar behavior while samples from different materials show different characteristics. However, no systematic dependence between the roughness characteristics (i)–(vi) and other production parameters such as the total number of layers N or the multilayer period d was found. Only the fractal exponent always decreases with the number of layers N in the structure. We determined roughness values for the substrate, for the average of all layer interfaces, and for the surface. In all samples the substrate had the lowest roughness values, the multilayer surface the highest, with the averaged interlayer roughness in between. From this we conclude that the roughness increases steadily from the substrate to the top layer surface.

For further investigation we used a roughness model described by Pietsch *et al.* (2004, p. 239). The increase of roughness is explained typically by two factors: (i) replication of the substrate roughness, and (ii) intrinsic roughness of every layer. Our model used in the simulations does not explain the replication effect and intrinsic roughness. Nevertheless, by comparing surface and interface roughnesses, vertical and lateral correlation lengths, the intrinsic roughness can be qualitatively estimated.

5.2.1. Pd/B_4C. The Pd/B_4C samples have the smallest surface and interface roughness of all materials investigated here. For the lateral roughness correlation we observe the shortest correlation lengths for the Pd/B_4C system. On the other hand, this system has the longest vertical correlation length of roughness. Moreover, the fractal exponent is close to 1 for this material and thus the fractal (topological) dimension $(3 - H)$ of the interface is close to 2. This means that every layer repeats in highest accuracy the surface structure of the underlying layer. In terms of growth model (Pietsch *et al.*, 2004, p. 239), we can state that for the Pd/B_4C system the replication of substrate roughness contributes more to the average roughness than in all other material systems. The intrinsic roughness plays the smallest role in this case.

5.2.2. W/Si. The W/Si system is a direct contrast to Pd/B_4C. Here, the vertical correlation of roughness has a lower impact. The roughness from an underlying layer is not reproduced well. The average fractal dimension of the interfaces is also far from 2. The difference between roughnesses A and B is not significant. Thus, the intrinsic roughness contribution is high. Concerning the average interface and surface roughness, this material system is placed between Pd/B_4C and Mo/Si. The roughness is better laterally correlated than for any other sample.

5.2.3. Mo/Si. The roughest material system is Mo/Si. These samples show generally the highest interface and surface roughness. The roughness replication is similar to W/Si and lower than for Pd/B_4C. Concerning the lateral correlation length, this material is placed between the two others.

5.3. Imaging and coherence

The stripe modulations present in the beam profile downstream of a multilayer are the main concern for high-resolution imaging applications. When comparing beam profiles of different synchrotron imaging facilities (*cf.* Fig. 1), one notices that, for example, the intensity or the sharpness of the modulations varies. Results of our study to shed light on the influence of the parameters of material combination, d-spacing and number of layers on the beam profile show the following.

For the material composition Pd/B_4C with a nominal d-spacing of 4.0 nm, specimens with 30 and 60 grown bi-layers are compared. Fig. 6 shows the stripe modulations for monochromatic illumination as well as the pseudo-polychromatic illumination for both samples (acquired at BM05, ESRF, 125 images were summed for the pseudo-polychromatic illumination). Additionally, vertical beam profiles are plotted as well as the reflectivity-*versus*-energy curves of the multilayers which were accessible within the same measurement owing to the scans of the energy performed. We note that changing the number of layers has no influence on the beam profile for this material composition and d-spacing. Increasing the numbers of layers changes the profile of the

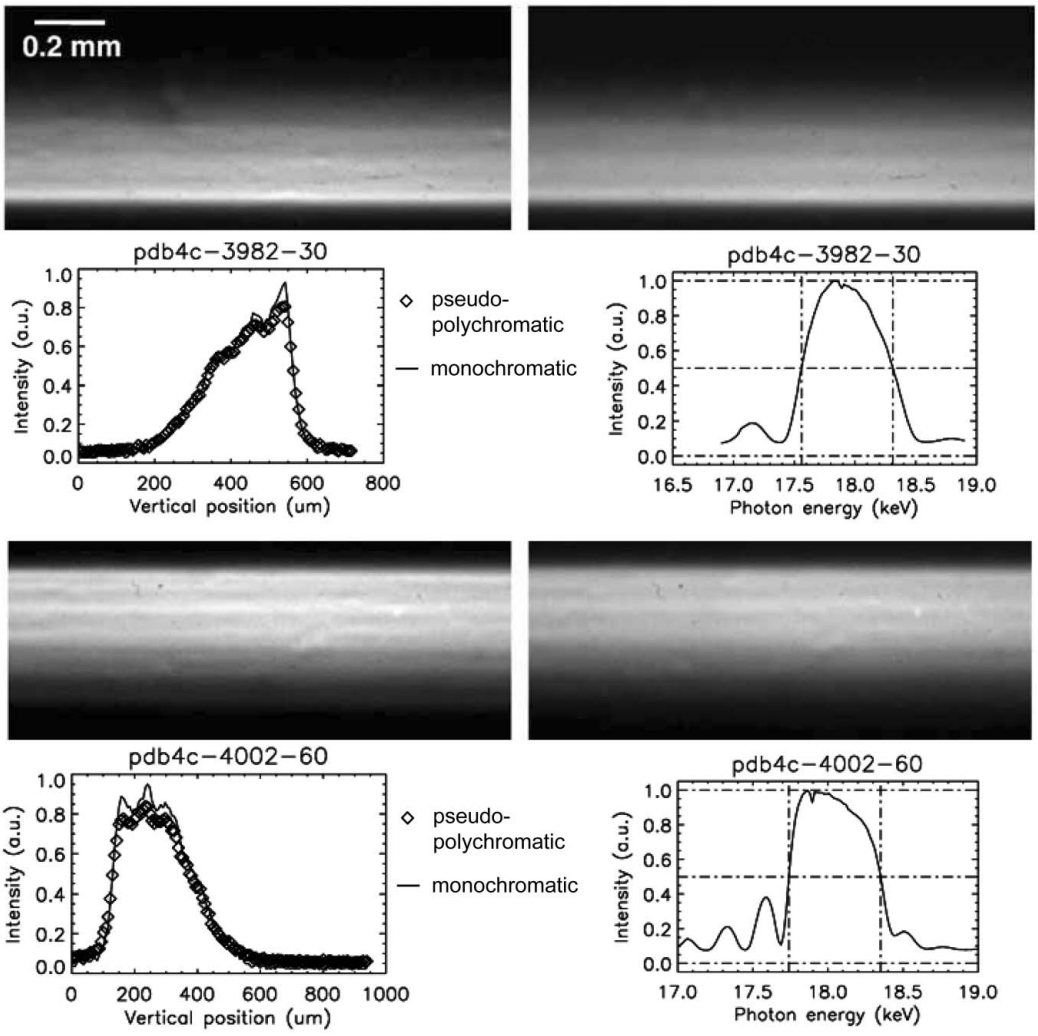

Figure 6
Influence of the number of grown layers on the beam profile, determined *via* the stripe modulations in full-field imaging (acquired at BM05, ESRF). Top: results for sample 1685 (Pd/B_4C, $N = 30$, $d = 3.982$ nm) (left: monochromatic illumination; right: polychromatic illumination). Bottom: results for sample 1681 (Pd/B_4C, $N = 60$, $d = 4.002$ nm).

reflectivity curve, as more bi-layers contribute at the given energy, resulting in a higher monochromaticity. Also, the asymmetry of the reflectivity curve for the mirror with 60 bi-layers is more pronounced owing to the variation of the penetration depth along the reflectivity curve and the higher total thickness of the multilayer. Between monochromatic and pseudo-polychromatic illumination one can recognise reduced noise as well as a slight blurring introduced by summing several images.

Similar results are observed in the case of keeping the material composition (Mo/Si) while modifying the *d*-spacing, as can be seen in Fig. 7. Three samples were investigated, with *d*-spacings of nominal 2.5 nm (220 bi-layers), 4.0 nm (80 bi-layers) and 5.5 nm (50 bi-layers). Based on the results obtained on Pd/B_4C (Fig. 6), we assume, in a first approximation, that the number of layers has no influence on the image quality. Therefore, the number of layers for these samples was chosen according to our energy range of interest, the number of bi-layers increasing when decreasing the *d*-spacing. For images taken with monochromatic illumination, similar stripe modulations are distinguishable for all three investigated multilayer structures. Changing the *d*-spacing seems to have a slight effect on the homogeneity of the image. For the pseudo-polychromatic illumination (150, 125 and 300 images summed up, respectively), results are identical except for the 5.5 nm (50 bi-layers) specimen. With respect to the other results we assume this to be an effect related to potential beam or monochromator instabilities which lead to a smearing out of the stripes. As an intermediate summary of these two sections we derive as a first result that the *d*-spacing has little influence and the number of layers has no influence on the stripe modulations.

Finally, in Fig. 8 images are shown for different material compositions (Mo/Si, W/Si, Pd/B_4C with 220, 120 and 220 bi-layers; 150, 300 and 95 images are summed for the pseudo-polychromatic illumination, respectively) but with a fixed *d*-spacing of nominal 2.5 nm. Contrary to the previous results, a rather strong variation of the stripe modulation when

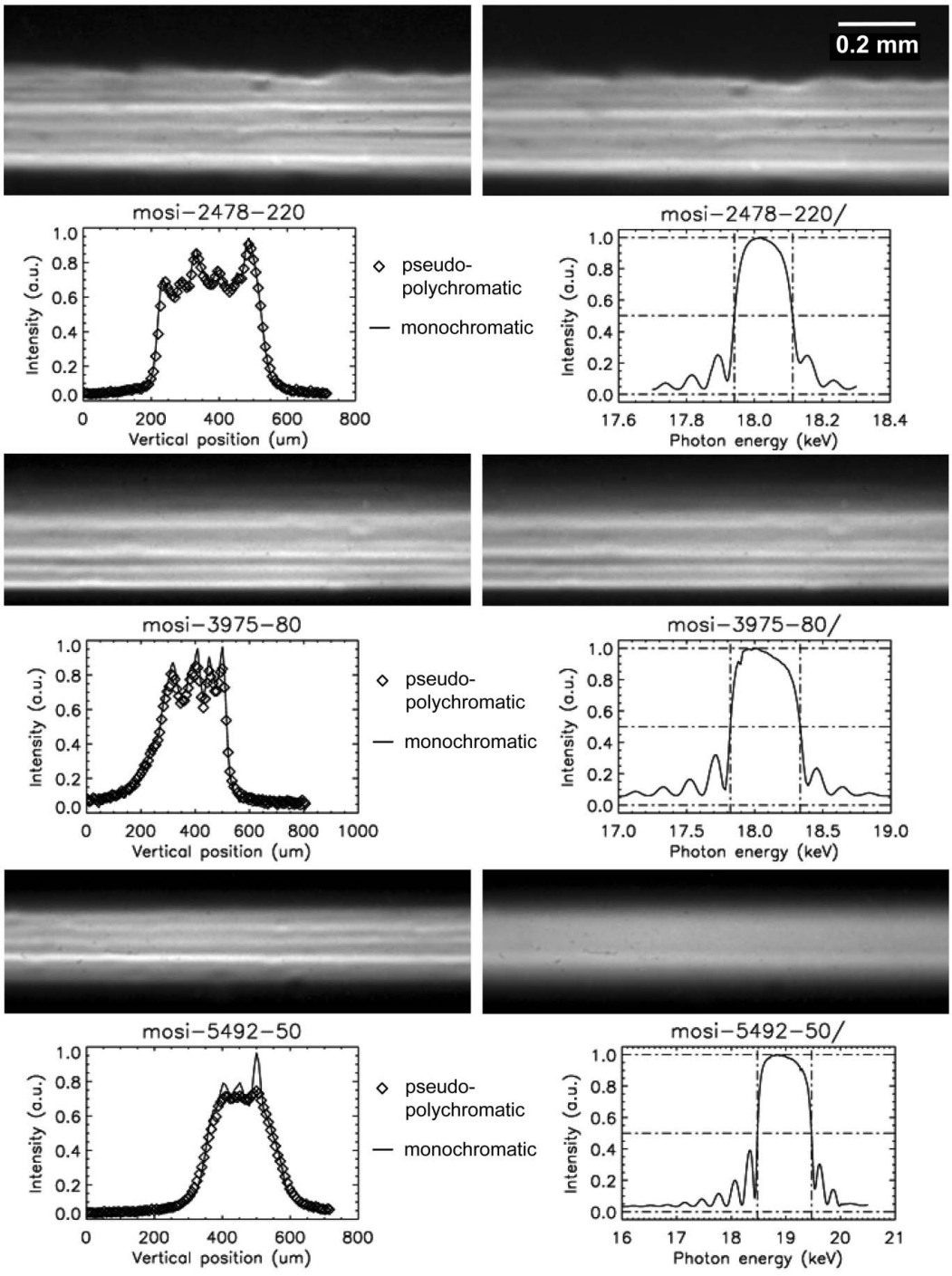

Figure 7
Influence of the *d*-spacing on the beam profile, determined *via* the stripe modulations in full-field imaging (left column: monochromatic illumination; right column: pseudo-polychromatic illumination, acquired at BM05, ESRF). Top: sample 1574 (Mo/Si, $N = 220$, $d = 2.478$ nm); middle: sample 1601 (Mo/Si, $N = 80$, $d = 3.975$ nm); bottom: sample 1609 (Mo/Si, $N = 50$, $d = 5.492$ nm) (bottom right image probably smeared owing to beam/crystal monochromator instabilities).

comparing different material compositions is visible. Mo/Si shows the strongest modulations in terms of the intensities of the stripes, while for Pd/B_4C the modulations in direct comparison with Mo/Si seem almost to disappear. W/Si ranges somewhere in between these two. We note that by visual comparison of the three images in Fig. 8 (independent of monochromatic or pseudo-polychromatic illumination) it seems that the more pronounced the stripe modulations in the image, the sharper the beam profile in general and *vice versa*.

For those three multilayer structures with differences in the stripe modulations of the reflected beam profile the influence of the beam modification on the achievable spatial resolution was measured. Results are displayed in Fig. 9 (acquired at the

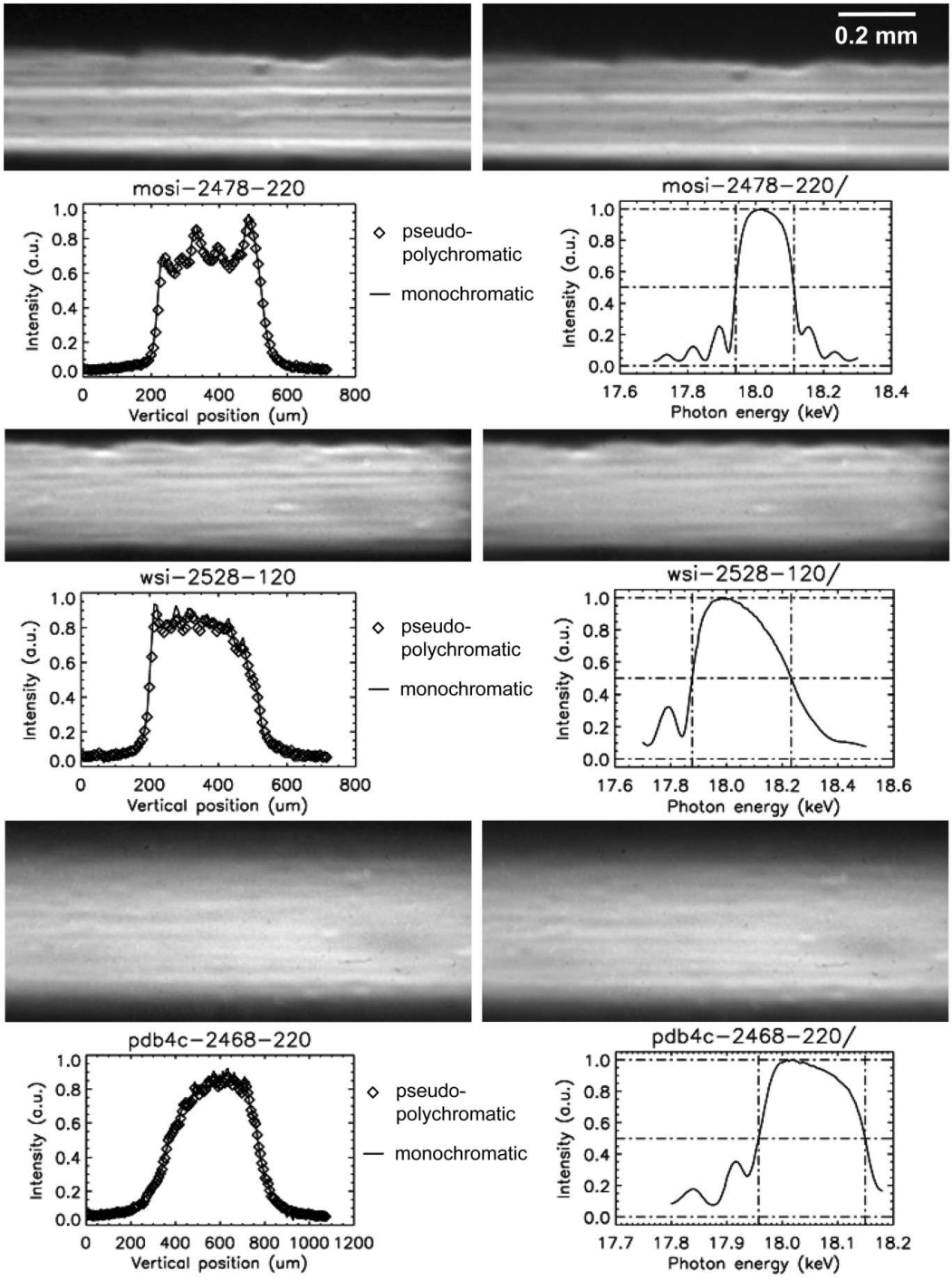

Figure 8
Influence of the material composition on the beam profile, determined *via* the stripe modulations in full-field imaging (left column: monochromatic illumination; right column: pseudo-polychromatic illumination, acquired at BM05, ESRF). Top: sample 1574 (Mo/Si, N = 220, d = 2.478 nm); middle: sample 1531 (W/Si, N = 120, d = 2.528 nm); bottom: sample 1680 (Pd/B_4C, N = 220, d = 2.468 nm). See also Figs. 9 and 10.

TopoTomo beamline, ANKA, Germany). For the image of the test pattern taken with the filtered white beam without multilayer an almost perfect flat-field correction is achieved. The smallest feature distinguishable on the one-dimensional test patterns is close to the 2.5 µm effective pixel size, hence the spatial resolution R reached here is determined by the spatial sampling rate of the detector (R > 5 µm; Shannon's theorem). In the test object the square in the lower-right corner contains a two-dimensional grid structure with 5 µm period. In the image taken without the multilayer, this area shows no structure at all: it appears almost homogeneously gray. The following images acquired using a beam reflected by one of the three multilayer structures are stitched in the vertical direction from several single images owing to the limited height of the reflected beam (the multilayer to test-pattern distance was approximately 1 m). In all three cases

the size of the smallest feature distinguishable on the one-dimensional test patterns is shifted to around 4 μm. This effect seems to be slightly less pronounced for Pd/B_4C in comparison with W/Si and Mo/Si. We explicitly note that this effect is not related to the stitching. The different quality of the applied flat-field correction is remarkable. While for Pd/B_4C and W/Si the background correction is almost as good as for the white beam, it is almost impossible to correct the background in the case of the Mo/Si multilayer. The reason for this remains unknown. Finally, the vertical lines of the grid structure in the lower-right square are clearly visible, strongly pronounced for, for example, Pd/B_4C. It can be concluded that the achievable spatial resolving power is similar for the three multilayer structures under investigation. Among the factors contributing to the different contrast observed with respect to the polychromatic illumination (blurring of the one-dimensional test patterns but higher visibility for the two-dimensional grid structure) are the more pronounced fringes (edge enhancement, inline phase contrast) owing to the monochromaticity of the reflected beam. Further conclusions are made difficult by the fact that the size of the grid test structure (lower-right square) is just at the limit given by Shannon's theorem, the pixel size being almost exactly half the period structure width, with the pixel grid aligned parallel to the test structure.

Besides the achievable spatial resolution, coherence properties of the reflected beam are important because coherent imaging techniques such as inline phase contrast or holotomography are applied more and more owing to their higher sensitivity. Results of the corresponding measurements can be found in Fig. 10 (performed at the ID19 beamline of the ESRF). As a reference, horizontal and vertical coherence properties of the beam as vertically reflected by a double-crystal monochromator only are shown. The multilayers affect essentially the vertical coherence properties as can be expected from the vertical reflection geometry. For Mo/Si, which had shown the strongest stripe modulations in the full-field image (not flat-field correctable), one finds that the coherence seems less affected by the reflection. For Pd/B_4C and in particular W/Si, which showed less pronounced stripe modulations (flat-field correctable), the coherence properties are significantly affected by the reflection.

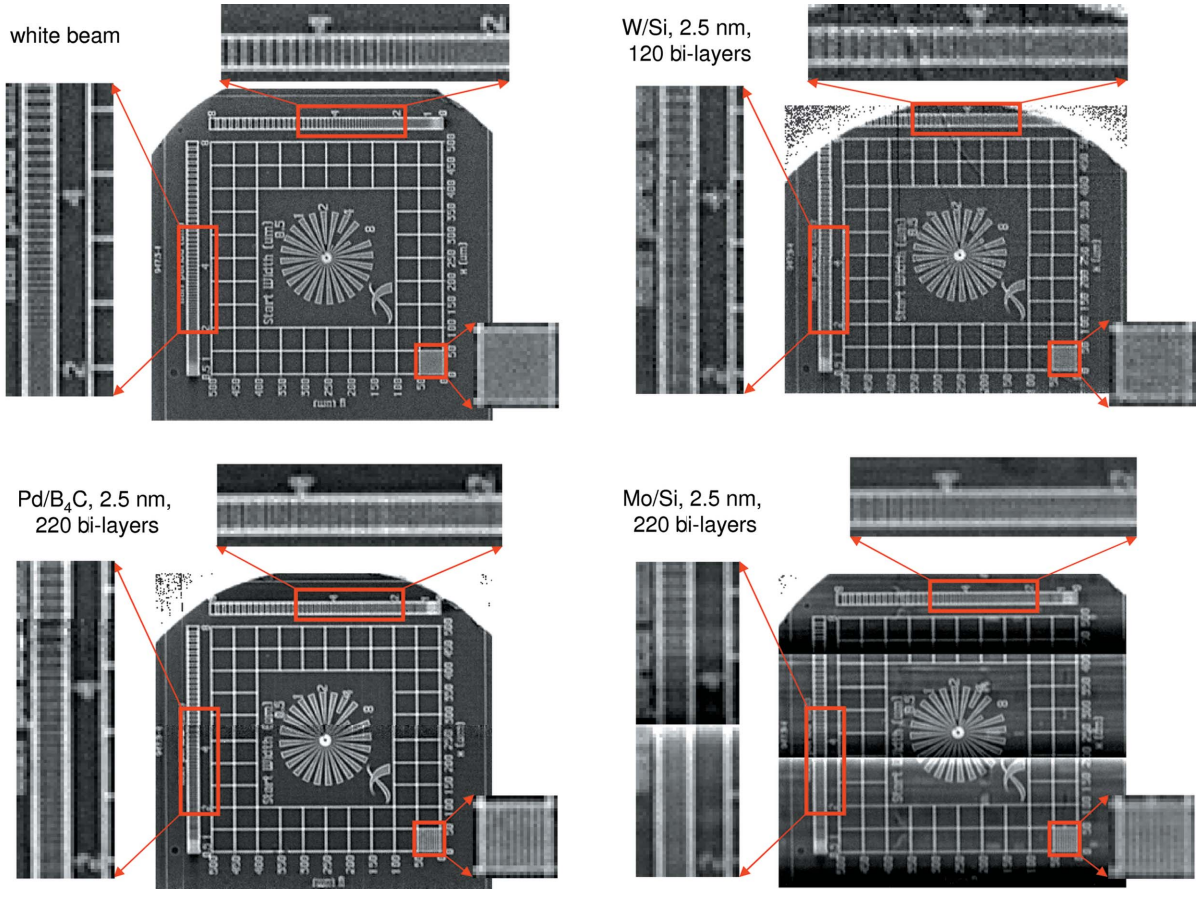

Figure 9
Flat- and dark-field-corrected images of a test pattern (Xradia, model X500-200-30) taken at the TopoTomo beamline (ANKA) utilizing an indirect detector with 2.5 μm effective pixel size (40 μm-thick CWO luminescence screen). The experiment was located approximately 30 m away from the source. Images were acquired as indicated using either the filtered white beam or after a multilayer reflection (18 keV). The images acquired with a monochromatic beam were stitched out of several single images owing to the limited height of the reflected beam (the multilayer to test-pattern distance was approximately 1 m; sample 1574: Mo/Si, N = 220, d = 2.478 nm; sample 1531: W/Si, N = 120, d = 2.528 nm; sample 1680: Pd/B_4C, N = 220, d = 2.468 nm). See also Figs. 8 and 10.

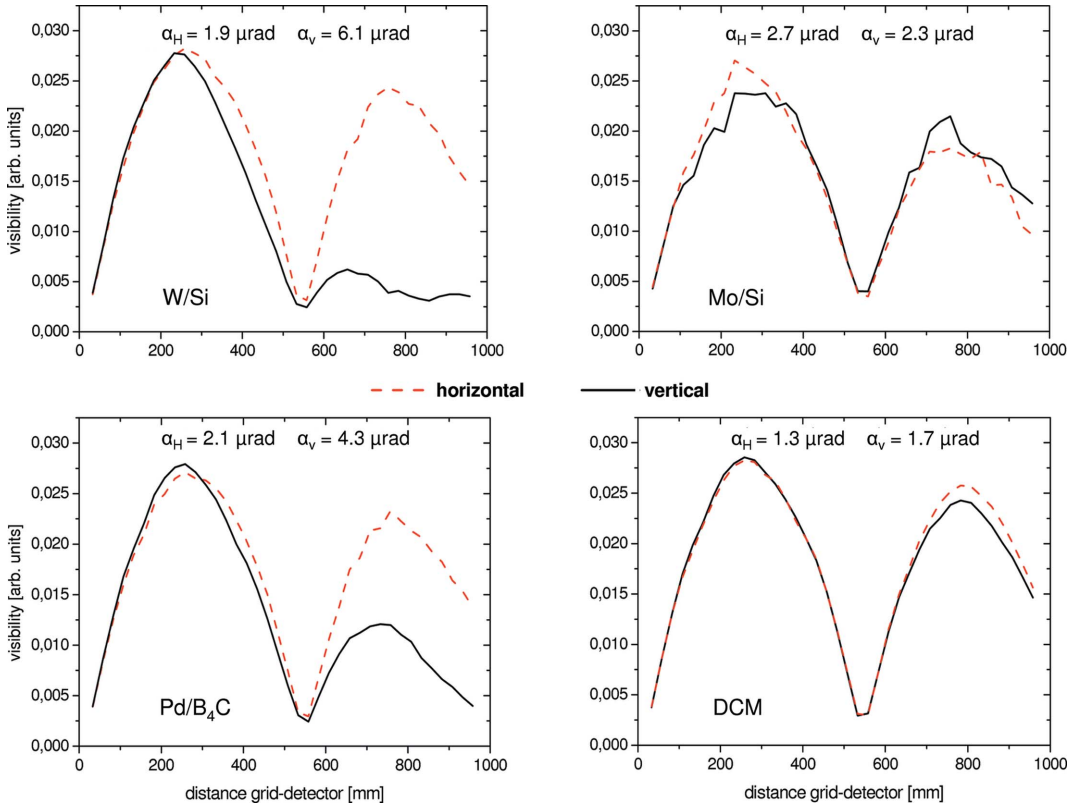

Figure 10
Coherence measurements as performed on ID19 (ESRF) *via* the visibility of a phase grating (Si, 6 µm periodicity) in dependence on its propagation distance to the detector. The beam passes a DCM (18 keV) before being reflected by one of the multilayer mirrors (sample 1574: Mo/Si, N = 220, d = 2.478 nm; sample 1531: W/Si, N = 120, d = 2.528 nm; sample 1680: Pd/B_4C, N = 220, d = 2.468 nm). Coherence properties of the beam when passing only the DCM are shown as well. The angular source size α is calculated from the two Talbot planes given (Cloetens *et al.*, 1997). See also Figs. 8 and 9.

6. Summary

We have presented a detailed characterization of multilayer structures as used for monochromators in coherent synchrotron-based hard X-ray micro-imaging. One of the major drawbacks of multilayer monochromatization, the irregular stripe pattern induced in the beam profile, showed a strong dependence on the material composition. From the three material compositions studied, Pd/B_4C showed the smoothest beam profiles, followed by W/Si. The third material system investigated, Mo/Si, showed strong stripe patterns. The number of bi-layers grown as well as the d-spacing showed a very small or almost negligible influence.

Furthermore, we used the Talbot effect to study the coherence properties of the beam as reflected by the three multilayer material compositions. Here we found a pronounced difference between the coherence properties of the beams reflected by different multilayer materials: the measurements showed that, while Mo/Si had the least effect on the coherence, W/Si affected it most, with Pd/B_4C in between.

In the simple model for qualitative explanation of the beam quality after reflection by a multilayer, the multilayer coating reproduces the underlying surface shape of the substrate. Intensity stripes downstream of the multilayer are caused by figure errors of the substrate that are reproduced by the multilayer coating. In observation planes far from the multilayer, these stripes can be washed out by the coherence loss owing to the roughness of the layers.

Since the substrates used in this study had comparable surface quality, the stripes in the beam profile should therefore, according to this model, be stronger for coatings with lower roughness. Likewise, the coherence should be best after those multilayer samples with the lowest roughness.

Surprisingly, this is not the case. For example, the Talbot effect measurements showed that, among the three materials systems investigated, Mo/Si preserves coherence best (while showing the strongest stripes). On the other hand, Pd/B_4C yields the smoothest beam profile, with the least pronounced stripes. This seems contradictory to the reflectometry results on roughness, which show that the three samples for which the coherence properties of the reflected beam were studied had similar roughness values.

We conclude that the models explaining the influence of a multilayer reflection on an X-ray wavefront need to be substantially expanded before they can correctly predict, even qualitatively, the influence of multilayer structure parameters on X-ray beam quality.

With respect to the achievable contrast and spatial resolution determined for the three compositions, we conclude that the sample made of Pd/B_4C, a materials system that had not been investigated with respect to hard X-ray imaging appli-

cations before, is the best suited among the three systems studied, at least for applications that do not require high-sensitivity phase contrast. It provides a rather smooth beam profile, allowing for an almost perfect flat-field correction. The coherence preservation characteristics, while poorer than for the Mo/Si sample, remain better than for the W/Si sample. It should be noted, however, that these conclusions cannot be considered generally valid for the materials composition as such, but only linked to the specific fabrication process parameters.

A reason for the poor flat-field correction in the Mo/Si images could be the particulary strong stripes in the beam profile from this test multilayer. Any drift of the beam position has a strong influence on the correction in this case. Even for a set-up with ideal mechanical stability the stripes will affect the correction quality because of the non-ideal point-spread function of the detector.

There are several aspects which are not covered by our study. The substrates used here are rather small (diameter 25.40 mm) and therefore their polishing quality may be better than what can easily be reached with substrates of the longer dimensions typically needed for imaging monochromators (several hundred millimeters length). However, practical experience shows that the large substrates can be produced with the same surface quality as smaller test samples. This was, for example, the case for the DMM at ESRF-BM05 (Bigault *et al.*, 2003) (Ru/B_4C from the ESRF multilayer laboratory and substrates from General Optics, Gooch & Housego) and for the more recent DMM at the TopoTomo beamline at ANKA (Pd/B_4C, W/Si from AXO Dresden GmbH, substrates from Carl Zeiss Laser Optics GmbH) (Rack *et al.*, 2010). Despite the strong effect on the coherence properties we found for W/Si, this material combination, albeit not always from the same manufacturer as the samples investigated here, as well as W/B_4C are applied successfully for coherent imaging techniques such as holotomography at the ID19 beamline (ESRF) as well as the BAM*line* (BESSY-II).

It should be noted that the performance of a multilayer monochromator at a beamline, and the quality of the beam at the sample position, are also strongly affected by the source dimensions and by the geometry of the beamline layout. This is independent of the composition and quality of the multilayer structures. A larger source size introduces blurring, which can be useful because it smears out the stripe pattern generated by the monochromator. In general, the closer the monochromator is to the source, and the further away it is located from the experimental station, the better the beam profile for a given quality of the multilayer (at the expense of higher flux density and heat load on the multilayer).

Further investigations based on the results we achieved could focus on the low-Z component, *i.e.* by comparing W/Si with W/B_4C for imaging applications. Some of the parameters might also be studied in a more reductionist manner, for example, by comparing material compositions with the same d-spacing and the same number of bi-layers, something that was not possible as part of this study. Of course, further materials compositions or refined process parameters should be investigated as well.

We acknowledge J.-Y. Massonnat (ESRF) for support during the beam time at BM05-ESRF, W. Ludwig (ESRF) for help during the beam time at ID19-ESRF, G. Buth (ANKA) during the beam time at SCD-ANKA, S. Zabler (TU Berlin) and C. David (PSI) for the phase gratings, and Francesco De Carlo (APS) for the flat-field image taken at 2BM-APS.

References

Banhart, J. (2008). *Advanced Tomographic Methods in Materials Research and Engineering.* Oxford University Press.
Baruchel, J., Buffiere, J.-Y., Cloetens, P., Di Michiel, M., Ferrie, E., Ludwig, W., Maire, E. & Salvo, L. (2006). *Scr. Mater.* **55**, 41–46.
Baruchel, J., Cloetens, P., Härtwig, J. & Schlenker, M. (2002). *Third-Generation Hard X-ray Synchrotron Radiation Sources*, edited by Dennis M. Mills, pp. 181–202. New York: John Wiley and Sons.
Bigault, T., Ziegler, E., Morawe, C., Hustache, R., Massonnat, J.-Y. & Rostaing, G. (2003). *Proc. SPIE*, **5195**, 12–20.
Bonse, U. & Busch, F. (1996). *Prog. Biophys. Mol. Biol.* **65**, 133–169.
Bonse, U., Nusshardt, R., Busch, F., Pahl, R., Johnson, Q. C., Kinney, J. H., Saroyan, R. A. & Nichols, M. C. (1989). *Rev. Sci. Instrum.* **60**, 2478–2481.
Brooks, R. A. & DiChiro, G. (1976). *Med. Phys.* **3**, 237–240.
Chu, Y. S., Liu, C., Mancini, D. C., De Carlo, F., Macrander, A. T., Lai, B. & Shu, D. (2002). *Rev. Sci. Instrum.* **73**, 1485–1487.
Cloetens, P., Barrett, R., Baruchel, J., Guigay, J.-P. & Schlenker, M. (1996). *J. Phys. D*, **29**, 133–146.
Cloetens, P., Guigay, J. P., De Martino, C., Baruchel, J. & Schlenker, M. (1997). *Opt. Lett.* **22**, 1059–1061.
Cloetens, P., Ludwig, W., Baruchel, J., Van Dyck, D., Van Landuyt, J., Guigay, J. P. & Schlenker, M. (1999). *Appl. Phys. Lett.* **75**, 2912–2914.
Conley, R., Liu, C., Qian, J., Kewish, C. M., Macrander, A. T., Yan, H., Kang, H. C., Maser, J. & Stephenson, G. B. (2008). *Rev. Sci. Instrum.* **79**, 053104.
Danilewsky, A. N., Rack, A., Wittge, J., Weitkamp, T., Simon, R., Riesemeier, H. & Baumbach, T. (2008). *Nucl. Instrum. Methods Phys. Res. B*, **266**, 2035–2040.
Danilewsky, A. N., Simon, R., Fauler, A., Fiederle, M. & Benz, K. W. (2003). *Nucl. Instrum. Methods Phys. Res. B*, **199**, 71–74.
David, C. & Hambach, D. (1999). *Microelectron. Eng.* **46**, 219–222.
Deschamps, P., Engström, P., Fiedler, S., Riekel, C., Wakatsuki, S., Høghøj, P. & Ziegler, E. (1995). *J. Synchrotron Rad.* **2**, 124–131.
Diaz, A., Mocuta, C., Stangl, J., Keplinger, M., Weitkamp, T., Pfeiffer, F., David, C., Metzger, T. H. & Bauer, G. (2010). *J. Synchrotron Rad.* **17**, 299–307.
Dietsch, R., Holz, Th., Mai, H., Hopfe, S., Scholz, R., Wehner, B. & Wendrock, H. (1995). *Mater. Res. Soc. Symp. Proc.* **382**, 345–350.
Dietsch, R., Holz, Th., Weißbach, D. & Scholz, R. (2002). *Appl. Surf. Sci.* **197–198**, 169–174.
Elliott, J. C. & Dover, S. D. (1982). *J. Microsc.* **126**, 211–213.
Flannery, B. P., Deckmann, H. W., Roberge, W. G. & D'Amico, K. L. (1987). *Science*, **237**, 1439–1444.
Flannery, B. P. & Roberge, W. G. (1987). *J. Appl. Phys.* **62**, 4668–4674.
Gawlitza, P., Braun, S., Dietrich, G., Menzel, M., Schädlich, S. & Leson, A. (2008). *Proc. SPIE*, **7077**, 707703.
Golub, L., Quillen, A. C. & Spiller, E. (1989). *Proc. SPIE*, **1160**, 176–180.
Görner, W., Hentschel, M. P., Müller, B. R., Riesemeier, H., Krumrey, M., Ulm, G., Diete, W., Klein, U. & Frahm, R. (2001). *Nucl. Instrum. Methods Phys. Res. A*, **467**, 703–706.
Graeff, W. & Engelke, K. (1991). *Handbook on Synchrotron Radiation*, edited by S. Ebashi, M. Koch and E. Rubenstein, pp. 361–406. Amsterdam: North-Holland.

Guigay, J.-P., Zabler, S., Cloetens, P., David, C., Mokso, R. & Schlenker, M. (2004). *J. Synchrotron Rad.* **11**, 476–482.
Ham, K., Jin, H., Butler, L. G. & Kurtz, R. L. (2002). *Rev. Sci. Instrum.* **73**, 1521–1523.
Harvey, J. E. (1995). *Appl. Opt.* **34**, 3715–3726.
Holý, V. & Baumbach, T. (1994). *Phys. Rev. B*, **49**, 10668–10676.
Holz, T., Dietsch, R., Mai, H. & Brügemann, L. (2000). *Mater. Sci. Forum*, **321**–**324**, 179–183.
Hsieh, J. (2009). *Computed Tomography: Principles, Design, Artifacts and Recent Advances*, 2nd ed. Bellingham: SPIE Press.
Jheon, S., Youn, H.-S., Kim, H.-T., Choi, G.-H. & Kim, J.-K. (2006). *Microsc. Res. Tech.* **69**, 656–659.
Kazimirov, A., Smilgies, D.-M., Shen, Q., Xiao, X., Hao, Q., Fontes, E., Bilderback, D. H., Gruner, S. M., Platonov, Y. & Martynov, V. V. (2006). *J. Synchrotron Rad.* **13**, 204–210.
Kewish, C. M., Assoufid, L., Macrander, A. T. & Qian, J. (2007). *Appl. Opt.* **46**, 2010–2021.
Kinney, J. H., Johnson, Q. C., Nichols, M. C., Bonse, U., Saroyan, R. A., Nusshardt, R. & Pahl, R. (1989). *Rev. Sci. Instrum.* **60**, 2471–2474.
Kluender, R., Masiello, F., van Vaerenbergh, P. & Härtwig, J. (2009). *Phys. Status Solidi A*, **206**, 1842–1845.
Koch, A. (1994). *Nucl. Instrum. Methods Phys. Res. A*, **348**, 654–658.
Koch, A., Raven, C., Spanne, P. & Snigirev, A. (1998). *J. Opt. Soc. Am.* **15**, 1940–1951.
Labiche, J.-C., Mathon, O., Pascarelli, S., Newton, M. A., Ferre, G. G., Curfs, C., Vaughan, G., Homs, A. & Carreiras, D. F. (2007). *Rev. Sci. Instrum.* **78**, 091301.
Lee, H.-R., Lai, B., Yun, W., Mancini, D. C. & Cai, Z. (1997). *Proc. SPIE*, **3149**, 257–264.
Liu, C., Macrander, A., Als-Nielsen, J. & Zhang, K. (2001). *J. Vac. Sci. Technol. A*, **19**, 1421–1424.
Mancini, D. C. & Bilderback, D. H. (1983). *Nucl. Instrum. Methods Phys. Res.* **208**, 263–272.
Moeckli, R., Verdun, F. R., Fiedler, S., Pachoud, M., Schnyder, P. & Valley, J.-F. (2000). *Phys. Med. Biol.* **45**, 3509–3523.
Montcalm, C., Kearney, P. A., Slaughter, J. M., Sullivan, B. T., Chaker, M., Pépin, H. & Falco, C. M. (1996). *Appl. Opt.* **35**, 5134–5147.
Morawe, Ch., Borel, Ch. & Peffen, J.-Ch. (2007). *Proc. SPIE*, **6705**, 670504.
Morawe, Ch. & Peffen, J.-Ch. (2009). *Proc. SPIE*, **7448**, 74480H.
Nagornaya, L., Onyshchenko, G., Pirogov, E., Starzhinskiy, N., Tupitsyna, I., Ryzhikov, V., Galich, Y., Vostretsov, Y., Galkin, S. & Voronkin, E. (2005). *Nucl. Instrum. Methods Phys. Res. A*, **537**, 163–167.
Pianetta, P., Barbee, T. W. & Redaelli, R. (1986). *Nucl. Instrum. Methods Phys. Res. A*, **246**, 352–355.
Pietsch, U., Baumbach, T. & Holý, V. (2004). *High-Resolution X-ray Scattering: From Thin Films to Lateral Nanostructures*, 2nd ed. Berlin: Springer.
Rack, A., García-Moreno, F., Baumbach, T. & Banhart, J. (2009*a*). *J. Synchrotron Rad.* **16**, 432–434.
Rack, A., Riesemeier, H., Vagovič, P., Weitkamp, T., Siewert, F., Dietsch, R., Diete, W., Bauer Trabelsi, S., Waterstradt, T. & Baumbach, T. (2010). *AIP Conf. Proc.* **1234**, 734–737.
Rack, A., Weitkamp, T., Bauer Trabelsi, S., Modregger, P., Cecilia, A. *et al.* (2009*b*). *Nucl. Instrum. Methods Phys. Res. B*, **267**, 1978–1988.
Rack, A., Zabler, S., Müller, B. R., Riesemeier, H., Weidemann, G., Lange, A., Goebbels, J., Hentschel, M. & Görner, W. (2008). *Nucl. Instrum. Methods Phys. Res. A*, **586**, 327–344.
Raven, C., Snigirev, A., Snigireva, I., Spanne, P., Souvorov, A. & Kohn, V. (1996). *Appl. Phys. Lett.* **69**, 1826–1828.
Reimers, P. & Goebbels, J. (1983). *Mater. Eval.* **41**, 732–737.
Riesemeier, H., Ecker, K., Görner, W., Müller, B. R., Radtke, M. & Krumrey, M. (2005). *X-ray Spectrom.* **34**, 160–163.
Riotte, M. (2008). Master's thesis, Universität Karlsruhe, Germany. [In German.]
Salditt, T., Metzger, T. H. & Peisl, J. (1994). *Phys. Rev. Lett.* **73**, 2228–2231.
Sammar, A., Krastev, K., André, J.-M., Barchewitz, R. & Rivoira, R. (1997). *Rev. Sci. Instrum.* **68**, 2969–2972.
Schelokov, I. A., Hignette, O., Raven, C., Snigirev, A. A., Snigireva, I. & Suvorov, A. (1996). *Proc. SPIE*, **2805**, 282–292.
Siewert, F., Lammert, H., Noll, T., Schlegel, T., Zeschke, T., Hänsel, T., Nickel, A., Schindler, A., Grubert, B. & Schlewitt, C. (2005). *Proc. SPIE*, **5921**, 592101.
Siewert, F., Noll, T., Schlegel, T., Zeschke, T. & Lammert, H. (2004). *AIP Conf. Proc.* **705**, 847–850.
Sijbers, J. & Postnov, A. (2004). *Phys. Med. Biol.* **49**, N247–N253.
Simon, R., Buth, G. & Hagelstein, M. (2003). *Nucl. Instrum. Methods Phys. Res. B*, **199**, 554–558.
Souvorov, A., Yabashi, M., Tamasaku, K., Ishikawa, T., Mori, Y., Yamauchi, K., Yamamura, K. & Saito, A. (2002). *J. Synchrotron Rad.* **9**, 223–228.
Spanne, P., Raven, C., Snigireva, I. & Snigirev, A. (1999). *Phys. Med. Biol.* **44**, 741–749.
Spanne, P. & Rivers, M. L. (1987). *Nucl. Instrum. Methods Phys. Res. B*, **24**–**25**, 1063–1067.
Spiller, E. (1980). *Nucl. Instrum. Methods*, **177**, 187–192.
Spiller, E. (1988). *J. Vac. Sci. Technol. A*, **6**, 1709–1710.
Spiller, E. (1994). *Soft X-ray Optics.* Bellingham: SPIE Press.
Spiller, E., Stearns, D. & Krumrey, M. (1993). *J. Appl. Phys.* **74**, 107–118.
Stampanoni, M., Groso, A., Isenegger, A., Mikuljan, G., Chen, Q., Meister, D., Lange, M., Betemps, R., Henein, S. & Abela, R. (2007). *AIP Conf. Proc.* **879**, 848–851.
Stock, S. R. (1999). *Int. Mater. Rev.* **44**, 141–164.
Stock, S. R. (2008). *Int. Mater. Rev.* **53**, 129–181.
Störmer, M., Horstmann, C., Häussler, D., Spiecker, E., Siewert, F., Scholze, F., Hertlein, F., Jäger, W. & Bormann, R. (2008). *Proc. SPIE*, **7077**, 707705.
Underwood, J. H. & Barbee, T. W. (1981). *Nature (London)*, **294**, 429–431.
Wang, Y., Liu, X., Im, K.-S., Lee, W.-K., Wang, J., Fezzaa, K., Hung, D. L. S. & Winkelman, J. R. (2008). *Nat. Phys.* **4**, 305–309.
Wang, Y., Narayanan, S., Liu, J., Shu, D., Mashayekhi, A., Qian, J. & Wang, J. (2007). *J. Synchrotron Rad.* **14**, 138–143.
Windt, D. L. (1998). *Comput. Phys.* **12**, 360–370.
Yamauchi, K., Yamamura, K., Mimura, H., Sano, Y., Saito, A., Endo, K., Souvorov, A., Yabashi, M., Tamasaku, K., Ishikawa, T. & Mori, Y. (2005). *Appl. Opt.* **44**, 6927–6932.
Ziegler, E. (1995). *Opt. Eng.* **34**, 445–452.
Ziegler, E., Hignette, O., Morawe, Ch. & Tucoulou, R. (2001). *Nucl. Instrum. Methods Phys. Res. A*, **467**–**468**, 954–957.
Ziegler, E., Hoszowska, J., Bigault, T., Peverini, L., Massonnat, J. Y. & Hustache, R. (2004). *AIP Conf. Proc.* **705**, 436–439.
Ziegler, E., Morawe, C., Hignette, O., Cloetens, P. & Tucoulou, R. (1999). *Ninth International Conference on Production Engineering, Precision Science and Technology for Perfect Surfaces*, Osaka, Japan, pp. 285–291.